

Deep inelastic scattering with the SPS muon beam*

Gerhard K. Mallot[†] and Rüdiger Voss[‡]
CERN, CH-1211 Geneva 23, Switzerland
[†]*gerhard.mallot@cern.ch*
[‡]*ruediger.voss@cern.ch*

Published 27 August 2015

We review results from deep inelastic muon scattering experiments at the SPS which started in 1978, and are still actively pursued today. Key results include the precision measurement of scaling violations and of the strong coupling constant, spin-dependent structure functions, and studies of the internal spin structure of protons and neutrons. These experiments have revealed a wealth of details about the internal structure of nucleons in terms of quarks and gluons.

1. Introduction

At the 14th International Conference in High Energy Physics in Vienna in 1968, SLAC reported for the first time the “scaling” behaviour of the electron–nucleon cross-section in the deep inelastic continuum, and W. K. H. Panofsky remarked that “. . . theoretical speculations are focused on the possibility that these data might give evidence on the behaviour of point-like, charged structures within the nucleon.”¹ Soon after, it was realised that the parton structure of the nucleon discovered by the first electron–nucleon scattering experiments in the deep inelastic regime indeed confirmed the quark model of Gell-Mann² and Zweig.³

The early SLAC results on the quark–parton structure of the nucleon had a profound impact on the first-generation experimental programme of the CERN Super Proton Synchrotron (SPS), and most notably on the muon and neutrino scattering experiments. Several groups realised the potential of this new machine to extend the landmark SLAC experiments much ‘deeper’ into the inelastic regime by building a high-intensity, high-energy muon beam. This was the beginning of one

*Also appeared in “60 Years of CERN Experiments and Discoveries”, eds. H. Schopper and L. Di Lella (World Scientific, 2015).

This is an Open Access article published by World Scientific Publishing Company. It is distributed under the terms of the Creative Commons Attribution 4.0 (CC-BY) License. Further distribution of this work is permitted, provided the original work is properly cited.

of the most prolific fixed-target physics programmes of CERN that started in 1978, soon after the commissioning of the SPS, and is still vigorously pursued today.

This brief review focuses on two central components of this programme which, from a present-day perspective, have had the most lasting impact: (a) the precision measurement of scaling violations for tests of perturbative QCD and measurements of the strong coupling constant, and (b) the measurement of spin-dependent structure functions, the discovery of the ‘spin crisis’, and comprehensive studies of the spin structure of the nucleon. However, it must not be overlooked that the CERN muon programme has, over the years, produced a wealth of other, sometimes unexpected results. Examples are the discovery of nuclear effects in deep inelastic scattering,⁴ the first observation of weak–electromagnetic interference effects in muon scattering, or measurements of charm production.

2. Beam and Detectors

The SPS muon beam M2⁵ was first commissioned in 1978 and is still in operation today, with only minor modifications. It is likely to be the best and most versatile high-energy muon beam ever designed, combining a wide range of momenta up to 300 GeV with high intensities and minimal halo background. The beam has a natural longitudinal polarisation that can be tuned by varying the momentum ratio of decay muons to parent pions, and can reach values up to $\approx 80\%$. A high beam polarisation is an essential prerequisite for the measurement of spin-dependent structure functions.

2.1. Early detectors

Two large detectors were built for the first generation of experiments, the NA2 experiment of the European Muon Collaboration (EMC),^{6–8} and the NA4 experiment of the Bologna–CERN–Dubna–Munich–Saclay (BCDMS) Collaboration.^{9,10} The two collaborations choose radically different, complementary experimental approaches. The EMC detector was a conventional open-geometry spectrometer built around a large air-gap dipole magnet, instrumented with proportional and drift chambers for particle tracking. The main advantages of this design were an excellent momentum resolution, a large kinematic range, and the ability to partly resolve the hadronic final state of the deep inelastic interaction. A disadvantage was the maximum target length allowed by the spectrometer layout, of order 1 m, which limits the statistical accuracy of many measurements.

In contrast, the BCDMS spectrometer was specifically designed for the inclusive measurement of high-momentum final state muons. It was based on a large, modular toroidal iron magnet of 50 m length instrumented with multiwire proportional chambers. In the centre, the toroid contained a modular target of almost the same length that could be filled with liquid hydrogen or deuterium, or replaced by solid target material. Principal advantages of this design were the enormous luminosity and the excellent muon identification through immediate absorption of the hadronic shower,

which could not be resolved by the detector. Another obvious drawback was the comparatively poor momentum resolution due to multiple scattering in the iron magnet, limited to $\Delta p/p \approx 10\%$ over most of the momentum range.

The EMC and BCDMS experiments took data from 1978 until 1985, both with liquid hydrogen, liquid deuterium, and solid nuclear targets. In addition, EMC made first measurements with a polarised solid ammonia target. Whereas the BCDMS spectrometer was subsequently dismantled, the more versatile EMC spectrometer underwent several upgrades, in particular for the later NMC (NA37, 1986–1989) and SMC (NA47, 1992–1996) experiments. The NMC Collaboration (where the N stands for “New”) refined and improved the EMC measurements of unpolarised structure functions, with a strong focus on the study of nuclear effects with a variety of heavy targets.¹¹ The SMC experiment (where the S stands for “Spin”, obviously) was devoted exclusively to polarised muon-nucleon scattering with solid butanol, deuterated butanol, and ammonia targets.

2.2. The COMPASS detector

The most comprehensive rebuild of the EMC/NMC/SMC spectrometer was undertaken by the COMPASS (NA58) Collaboration, which today continues the successful tradition of muon scattering at CERN, and still uses some of the original EMC equipment. The COMPASS experiment¹² started taking data in 2002.

Contrary to the one-stage EMC⁶ and SMC spectrometers, the COMPASS detector (Fig. 1) is a two-stage magnetic spectrometer with the SM1 and SM2 dipoles. This results in a very large acceptance which is important for semi-inclusive deep inelastic scattering (SIDIS) experiments. Other essential additions and improvements concern the particle identification detectors, the large-acceptance, superconducting target magnet, and last but not least the high rate and data acquisition capabilities, which went up from the order of 100 Hz to 25 kHz.

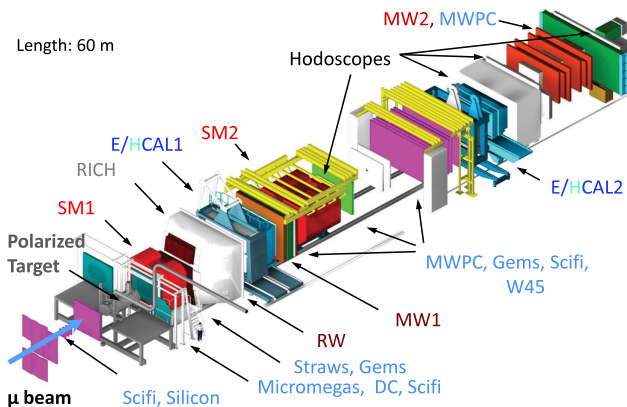


Fig. 1. Artist’s view of the COMPASS spectrometer. For a description see the text.

The COMPASS spectrometer is installed in the M2 muon beam line delivering muons of 160–200 GeV with a polarisation of about 80%. The usable beam intensity is typically 2×10^7 /s during a 9.6 s long spill. The repetition rate varies and is typically about 1/40 s. The momentum of each beam muon is measured in the beam momentum station.

Charged particles are tracked in the beam region by scintillating fibre stations (SciFi) and silicon detectors. In the region close to the beam, micromega and gas-electron-multiplier (GEM) gaseous detectors with high rate capabilities are deployed. The backbone of tracking in the intermediate region is formed by multi-wire proportional chambers (MWPCs). Finally, the large area tracking is covered by drift chambers (DC, W45) and drift tubes (Straws, RW, MW).

The velocity of charged particles is measured in a ring-imaging Cherenkov detector (RICH), which can separate pions and kaons from 9 GeV up to 50 GeV. The photon detector comprises multianode-photomultiplier tubes and in the periphery MWPCs with photosensitive CsI cathodes. The energy of charged particles is measured in sampling hadron calorimeters (HCAL), while neutral particles, in particular high-energy photons, are detected in electromagnetic calorimeters (ECAL).

Event recording is triggered by the scattered muon, which is “identified” by its ability to traverse thick hadron absorbers located just upstream of the Muon Wall detectors (MW), and detected by various systems of scintillator hodoscopes. The same spectrometer is also used for an experimental programme on hadron spectroscopy using pion, kaon and proton beams.¹³

2.3. *The COMPASS polarised target*

The heart of the experiment is the superconducting polarised target system. It comprises a 2.5 T solenoid and a 0.6 T dipole magnet, a $^3\text{He}/^4\text{He}$ dilution refrigerator originating from SMC, a 70 GHz microwave system for the dynamic nuclear polarisation (DNP), and an NMR system to measure the target polarisation. The target material is cooled down to about 60 mK in frozen spin mode. Irradiated ammonia (NH_3) and lithium-6 deuteride (^6LiD) were selected as proton and deuteron targets, respectively. Typical polarisations achieved are 85% for protons and 50% for deuterons. The target volume has an overall length of 1.3 m and comprises two or three cells with opposite polarisations. The target spins are rotated typically once per day by rotation of the magnetic field vector. The rotation can be stopped in transverse position for measurements with transverse target polarisation. For such measurements the polarisation is inverted typically once per week by DNP.

3. Unpolarised Nucleon Structure Functions

Deep inelastic lepton–nucleon scattering is loosely defined as scattering at energy transfers much larger than the parton binding energy in the nucleon, such that the interaction occurs at the parton level and thus probes the internal quark–parton structure of the target nucleon. Charged lepton scattering can be mediated through

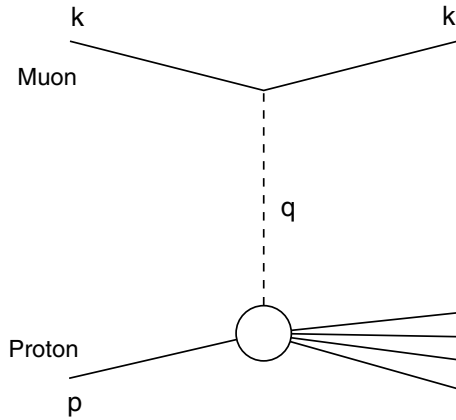


Fig. 2. Deep inelastic muon–nucleon scattering in lowest order.

neutral-current γ or Z exchange, or through charged current W^\pm exchange. At typical SPS fixed-target energies of a few hundred GeV, it is dominated by single photon exchange (Fig. 2). Consequently, muon scattering at CERN has mostly focused on this channel. The excellent luminosity of the BCDMS spectrometer has allowed for measurements of γ – Z interference^{14,15} which however have been completely superseded by data from HERA, and are not reviewed here.

3.1. Cross-section and structure functions

For inclusive scattering where the scattering amplitudes are summed over all possible hadronic final states, the unpolarised cross-section can be written as a function of two independent kinematic variables. One usually chooses two of the following Lorentz invariant variables,

- the squared four-momentum transfer

$$Q^2 = -q^2 = -(k - k')^2 = 4EE' \sin^2 \theta; \quad (1)$$

- the energy transfer to the hadronic system

$$\nu = \frac{p \cdot q}{M} = E' - E; \quad (2)$$

- the Bjorken scaling variable

$$x = \frac{Q^2}{2p \cdot q} = \frac{Q^2}{2M\nu}; \quad (3)$$

- and the scaling variable

$$y = \frac{p \cdot q}{p \cdot k} = \frac{\nu}{E}. \quad (4)$$

In these equations, k , k' , p and q are the four-vectors of the initial and final state lepton, the target nucleon, and the exchanged boson. M is the mass of the target nucleon and the lepton mass has been neglected. E , E' , and θ are the energies of the incident and scattered lepton, and the lepton scattering angle, in the laboratory frame.

The differential cross-section for unpolarised deep inelastic charged lepton scattering can be written, in the Born approximation, as^{16,17}

$$\frac{d^2\sigma}{dQ^2 dx} = \frac{4\pi\alpha^2}{Q^4} \frac{1}{x} \left[xy^2 F_1(x, Q^2) + \left(1 - y - \frac{Mxy}{2E} \right) F_2(x, Q^2) \right], \quad (5)$$

where α is the electromagnetic coupling constant and $F_1(x, Q^2)$ and $F_2(x, Q^2)$ are the unpolarised structure functions of the nucleon,

$$F_1(x, Q^2) = \frac{1}{2x} \sum_i e_i^2 x q_i(x, Q^2), \quad (6)$$

$$F_2(x, Q^2) = 2xF_1(x, Q^2) = \sum_i e_i^2 x q_i(x, Q^2). \quad (7)$$

In these expressions, $q_i(x, Q^2)$ is the probability distribution of partons of flavour i in the kinematic variables x and Q^2 and the index i runs over the active parton flavours in the nucleon. The SLAC discovery that the structure functions depend, at least approximately, on the dimensionless scaling variable x only,^{18,19}

$$q_i(x, Q^2) \approx q_i(x) \quad (8)$$

— the effect commonly referred to as “scaling” — is interpreted in the Quark-Parton Model (QPM) as elastic scattering on dimensionless, i.e. pointlike scattering centres inside the nucleon. Scaling becomes exact in the Bjorken limit where Q^2 , $\nu \rightarrow \infty$ at constant x ,²⁰ such that the transverse momentum of partons in the infinite momentum frame of the proton becomes negligible.

3.2. Scaling violations

When the muon experiments at the SPS started taking data in 1978, scaling and the QPM were well established experimentally and phenomenologically. The key interest of the experiments shifted soon to the measurement of small deviations from exact scaling behaviour, or *scaling violations*. As an example, the most representative fixed-target measurements of the proton structure function $F_2^p(x, Q^2)$ are shown in Fig. 3.^a They exhibit a characteristic rise of the structure function with Q^2 at small x , a decrease at large x , and “apparent scaling” at $x \approx 0.15$.

^aThe first-generation data from muon scattering at the SPS were plagued by significant disagreements between the EMC and BCDMS results on F_2 . The NMC Collaboration later remeasured this structure function with the upgraded EMC spectrometer, and eventually confirmed the BCDMS results.

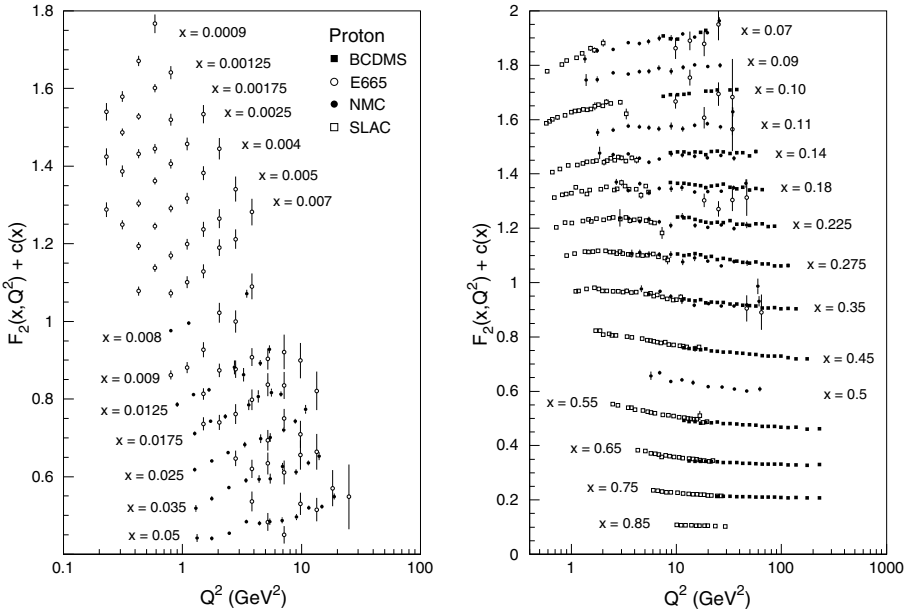


Fig. 3. The proton structure function F_2^P measured in deep inelastic muon scattering by the BCDMS²¹ and NMC²² experiments, shown as a function of Q^2 for bins of fixed x . The CERN data are complemented at small Q^2 by the SLAC electron scattering data,²³ and at small x by muon scattering data from the Fermilab E665 experiment.²⁴ Only statistical errors are shown. For the purpose of plotting, a constant $c(x) = 0.1i_x$ is added to F_2^P where i_x is the number of the x bin, ranging from 1 ($x = 0.05$) to 14 ($x = 0.0009$) on the left-hand figure, and from 1 ($x = 0.85$) to 15 ($x = 0.007$) on the right-hand figure.

3.3. Tests of perturbative QCD

Scaling violations occur naturally in Quantum Chromodynamics since, at large parton momenta x and increasing Q^2 , the structure functions are increasingly depleted by hard gluon radiation from quarks; at small x , they are enriched by gluon conversion into low-momentum quark–antiquark pairs. The initial years of experimentation with the SPS muon beam coincided with the emergence of QCD as the universally accepted theory of the strong interaction, and were an active and exciting period of cross-fertilisation of phenomenology and experiments. Precise data on scaling violations turned out to be one of the most powerful tools to test the perturbative branch of the new theory, and allowed for one of the best early measurements of the strong coupling constant.

The Q^2 evolution of the strong coupling constant α_s is controlled by the renormalisation group equation of QCD. The “canonical” — but by no means unique — solution usually adopted for the analysis of deep inelastic data is, in next-to-leading order (NLO),

$$\alpha_s(Q^2) = \frac{4\pi}{\beta_0 \ln(Q^2/\Lambda^2)} \left[1 - \frac{\beta_1}{\beta_0^2} \frac{\ln \ln(Q^2/\Lambda^2)}{\ln(Q^2/\Lambda^2)} \right] \quad (9)$$

where the so-called beta functions are given by

$$\beta_0 = 11 - \frac{2}{3}N_f, \quad \beta_1 = 102 - \frac{38}{3}N_f$$

and N_f is the effective number of active quark flavours in the scattering process. The parameter Λ is the so-called “mass scale” of QCD and has the physical meaning of a typical energy at which the running coupling constant (9) becomes large and the perturbative expansion breaks down. Its value is not predicted by QCD and can only be determined by experiment. Since α_s is the physical observable, the numerical value of Λ depends on N_f and, beyond leading order, on the renormalisation scheme assumed to compute the perturbative QCD expansions.

The Q^2 evolution of the effective quark and gluon distribution is predicted by the Altarelli–Parisi equations,²⁵

$$\frac{dq^{NS}(x, Q^2)}{d \ln Q^2} = \frac{\alpha_s(Q^2)}{2\pi} \int_x^1 q^{NS}(t, Q^2) P^{NS}\left(\frac{x}{t}\right) \frac{dt}{t}, \quad (10)$$

$$\frac{dq^{SI}(x, Q^2)}{d \ln Q^2} = \frac{\alpha_s(Q^2)}{2\pi} \int_x^1 \left[q^{SI}(t, Q^2) P_{qq}\left(\frac{x}{t}\right) + C_q g(t, Q^2) P_{qg}\left(\frac{x}{t}\right) \right] \frac{dt}{t}, \quad (11)$$

$$\frac{dg(x, Q^2)}{d \ln Q^2} = \frac{\alpha_s(Q^2)}{2\pi} \int_x^1 \left[g(t, Q^2) P_{gg}\left(\frac{x}{t}\right) + C_g q^{SI}(t, Q^2) P_{gq}\left(\frac{x}{t}\right) \right] \frac{dt}{t}, \quad (12)$$

where SI and NS denote flavour singlet and non-singlet combinations of quark distributions, respectively, g is the gluon distribution, and the C_i are a set of coefficients. P^{NS} , P_{qq} , etc. are so-called splitting functions describing the QCD diagrams which can be calculated in perturbative QCD as power series in α_s .

3.4. Measurement of the strong coupling constant

The F_2 measurements of BCDMS at large x and Q^2 with carbon, hydrogen, and deuterium targets were the first high statistics data that yielded a conclusive determination of Λ_{QCD} .^{26–28} The original BCDMS fits to the hydrogen and deuterium data were later superseded by a careful analysis by Virchaux and Milsztajn of the combined SLAC and BCDMS hydrogen and deuterium data.²⁹ Since the SLAC data extend down to four-momentum transfers as low as $Q^2 = 1 \text{ GeV}^2$, these authors make an allowance for non-perturbative “higher twist” contributions to the observed scaling violations at small Q^2 . These higher twist effects are mostly due to long-distance final state interactions which are difficult to calculate in perturbative QCD and there is little theoretical prejudice about their kinematical dependence except that they can be expanded into power series in $1/Q^2$.³⁰ This suggests an *ansatz*

$$F_2(x, Q^2) = F_2^{LT}(x, Q^2) \left[1 + \frac{C_{HT}(x)}{Q^2} \right] \quad (13)$$

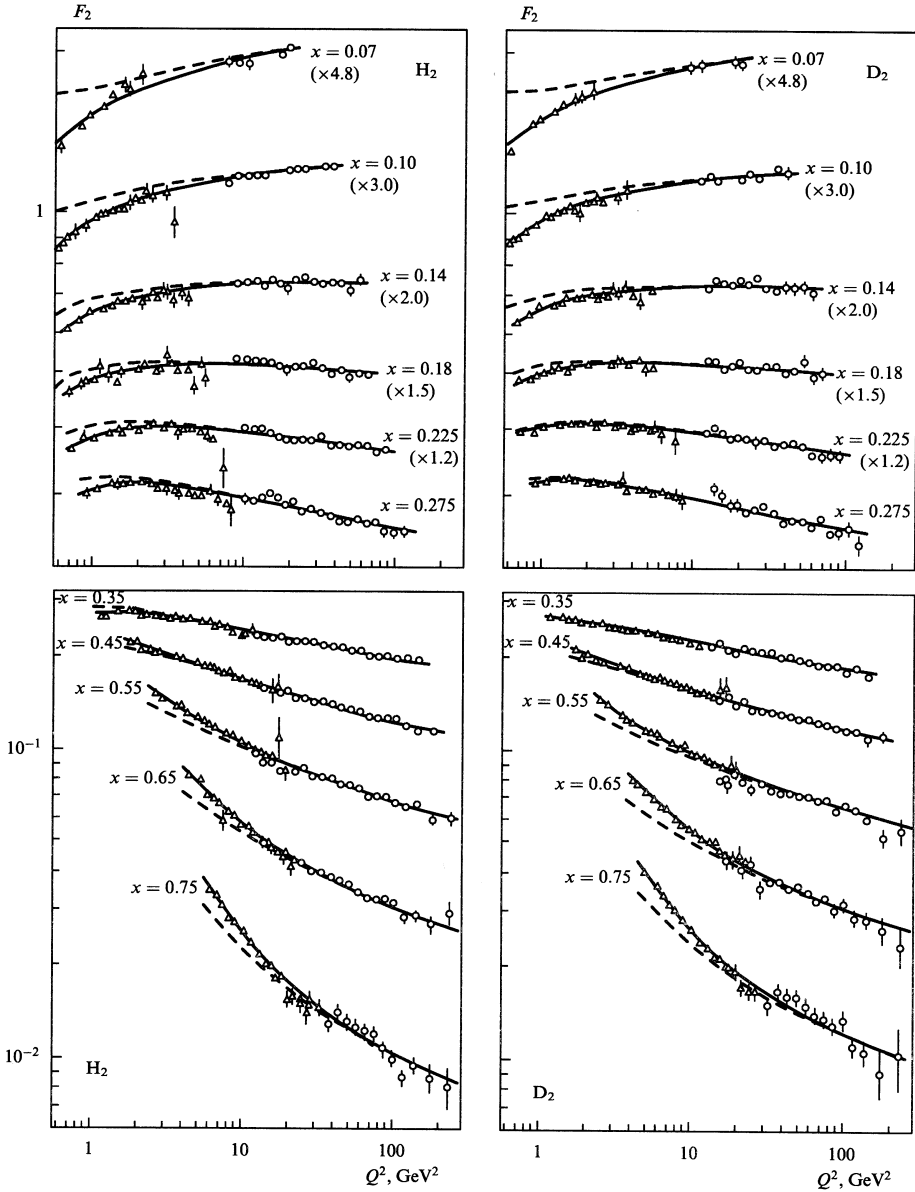


Fig. 4. QCD fit to the SLAC (triangles) and BCDMS (circles) data on $F_2(x, Q^2)$. The dashed line is the purely perturbative fit with the leading twist structure function $F_2^{LT}(x, Q^2)$. The solid line includes the higher twist contribution discussed in the text.

where the leading twist structure function F_2^{LT} follows the Altarelli–Parisi equations, and which gives indeed a very satisfactory fit to the data (Fig. 4). The quality of the fit is best illustrated in the representation of the “logarithmic slopes” which shows the derivative of the structure function with respect to $\ln Q^2$ as predicted by

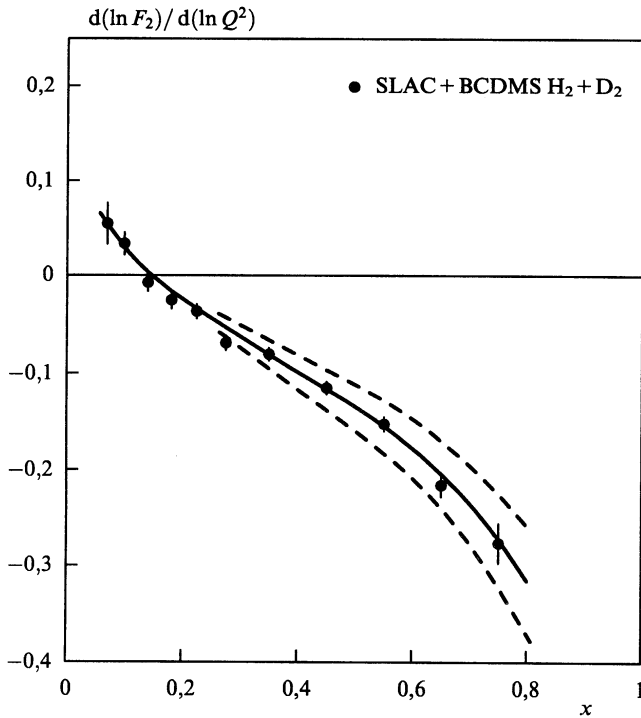


Fig. 5. Scaling violations $d \ln F_2/d \ln Q^2$ observed in the combined SLAC/BCDMS hydrogen and deuterium data. Errors are statistical only. The solid line is a QCD fit corresponding to $\alpha_s(M_Z^2) = 0.113$; the dashed lines correspond to $\Delta\alpha_s(M_Z^2) = 0.010$.

the Altarelli–Parisi equations, averaged over the Q^2 range of each bin in x (Fig. 5). In this analysis, the higher twist term $C_{HT}(x)$ of Eq. (13) is fitted by a set of constants in each bin of x . These coefficients are compatible with zero for $x < 0.4$, i.e. perturbative QCD can describe scaling violations in this region down to Q^2 as small as 1 GeV^2 .

In the same analysis, Virchaux and Milsztajn have also estimated the “theoretical” uncertainty due to the neglect of higher order terms in the perturbative QCD expansions. Their final result for α_s at $Q^2 = M_Z^2$ is

$$\alpha_s(M_Z^2) = 0.113 \pm 0.003 \text{ (exp.)} \pm 0.004 \text{ (theor.)} .$$

A later analysis by Alekhin³¹ based on the combined SLAC, BCDMS, and NMC data yielded $\alpha_s(M_Z^2) = 0.1183 \pm 0.0021 \text{ (exp.)} \pm 0.0013 \text{ (theor.)}$. These data still provide significant input to the present world average of α_s from deep inelastic scattering, and are in good agreement with the final combined result from LEP.³²

As a byproduct, these QCD fits can also provide an estimate of the gluon distribution in the nucleon (Eq. (11)). Since the gluon distribution is strongly peaked at small x , however, this estimate is now superseded by fits to more recent data, in particular data from HERA, with better coverage of this kinematic region.

4. Nucleon Spin and Polarised Deep Inelastic Scattering

One of the last experiments performed by the EMC was in 1985 the measurement of the double-spin cross-section asymmetry for inclusive deep inelastic scattering of longitudinally polarised muons off longitudinally polarised protons. As in the unpolarised case initial measurements had been performed at SLAC at lower energies in a limited kinematic range. While the SLAC measurements were in line with expectations from the QPM, the EMC results showed in the previously unmeasured small- x region ($x < 0.1$) a clear disagreement with potentially dramatic consequences.^{33,34} In the QPM, the nucleon spin is supposed to arise entirely from the quark spins, while in relativistic quark models a contribution of about 60% is expected. However, the EMC result was compatible with zero. Leader and Anselmino conclude in 1988³⁵ in an article entitled “A crisis in the parton model: where, oh where is the proton’s spin?”:

- (a) Orbital angular momentum may be important; and this is perfectly consistent with what is known about the intrinsic k_T [transverse momentum] of quarks.
- (b) The sacrosanct Bjorken sum rule may be broken. A measurement of g_1^n [of the neutron] is clearly now vital!
- (c) The experiment may be wrong. Given its fundamental importance it should be redone . . . obviously, with great emphasis on the small x region.

The unexpected result, dubbed the spin crisis, gave birth to many new experiments, including those of the Spin Muon (SMC) and COMPASS Collaborations at CERN. A very fruitful interplay between theory and experiment enrolled opening up a whole field of research now extending to transverse polarisation, transverse-momentum dependent (TMD) and generalised parton distributions (GPD). A comprehensive recent review is presented in Ref. 36 including non-CERN work by HERMES at DESY, Jefferson Lab and the Relativistic Heavy Ion Collider (RHIC) at the Brookhaven National Laboratory not covered here.

4.1. Longitudinal spin

The spin of the nucleon of $1/2$ (in units of \hbar) can be decomposed into contributions from spins ‘ Δ ’ and orbital angular momenta L from both quarks q and gluons g

$$\frac{1}{2} = \frac{1}{2} \Delta\Sigma + \Delta g + L_g + L_q, \quad (14)$$

with

$$\Delta\Sigma = \Delta u + \Delta d + \Delta s + \text{aq.}, \quad (15)$$

where “aq.” indicates the corresponding terms for antiquarks. The individual spin contributions from the up, down, and strange quarks to the nucleon spin are given by

the first moments Δu , Δd , and Δs of the corresponding helicity distributions $\Delta q_i(x)$

$$\Delta i = \int_0^1 \Delta q_i(x) dx \quad \text{with } i = u, d, s, \text{ and antiquarks,} \quad (16)$$

where

$$\Delta q_i(x) = q_i^+(x) - q_i^-(x). \quad (17)$$

Here, the superscripts + and - denote the helicity of the quarks; the gluon helicity distribution $\Delta g(x)$ is defined accordingly. While in the unpolarised case the sum $q_i(x) = q_i^+(x) + q_i^-(x)$ of the number densities of quarks appears, in the polarised case this role is taken by their difference.

The quark helicity distributions $\Delta q_i(x, Q^2)$ in the nucleon can be accessed via the spin-dependent structure function $g_1(x, Q^2)$, which appears in the DIS cross-section. In the QPM the structure function g_1 is given by

$$g_1(x) = \frac{1}{2} \sum_i e_i^2 \Delta q_i(x), \quad (18)$$

where e_i denotes the electric charge of the struck quark (compare Eq. (6)). Like F_1 , also g_1 depends on Bjorken x and logarithmically on Q^2 .

4.1.1. Sum rules

For the proton the first moment Γ_1 of g_1 can be decomposed into three axial charges: the isovector charge a_3 , the octet charge a_8 and the flavour-singlet charge a_0

$$\Gamma_1^p(Q^2) = \int_0^1 g_1^p(x, Q^2) dx = \frac{1}{12} \left(a_3 + \frac{1}{3} a_8 \right) + \frac{1}{9} a_0. \quad (19)$$

They are given in terms of flavour contributions by

$$a_3 = \Delta u - \Delta d + aq., \quad a_8 = \Delta u + \Delta d - 2\Delta s + aq., \quad a_0 = \Delta u + \Delta d + \Delta s + aq. \quad (20)$$

The isovector and isoscalar charges come with Q^2 -dependent Wilson coefficients, which are calculable in perturbative QCD and are omitted here. For the Q^2 -dependent flavour-singlet axial charge a_0 usually its normalisation-scheme independent value at $Q^2 \rightarrow \infty$ is quoted. In the $\overline{\text{MS}}$ renormalisation scheme, a_0 is identical to $\Delta\Sigma$, the sum of all quark spins (Eq. (15)). However, while a_0 is an observable, $\Delta\Sigma$ *per se* is not. The isovector axial charge a_3 is equal to the weak coupling constant $|g_A/g_V|$ measured independently in neutron decay and a_8 is known from hyperon decays assuming SU(3) flavour symmetry. Both are Q^2 independent.

Subtracting from Eq. (19) the corresponding equation for the neutron yields the fundamental Bjorken sum rule^{37,38} which for $Q^2 \rightarrow \infty$ reads

$$\Gamma_1^p - \Gamma_1^n = \frac{1}{6} \left| \frac{g_A}{g_V} \right|. \quad (21)$$

The a_0 and a_8 axial charges cancel in the difference of proton and neutron, i.e. when Δu is replaced by Δd and vice versa. This famous sum rule links the first moment of the structure function g_1 (for $Q^2 \rightarrow \infty$) to the neutron decay constant and was derived already in 1966 using current algebra. However, Bjorken first dismissed it as a ‘worthless’ equation, because performing a measurement with a polarised neutron target seemed impossible at the time. Only three years later he reconsidered this statement “in light of the present experimental and theoretical situation”. It took until 1992 that the first neutron (deuteron and helium-3) measurements were performed. Earlier proposals to measure the neutron as part of the E130 experiment at SLAC were finally not carried out. At this time the proton results were in line with expectations and thus a neutron measurement was less pressing.

In 1973, Ellis and Jaffe used Eq. (19) to make a prediction³⁹ for Γ_1 assuming an unpolarised strange sea ($\Delta s = 0$) in which case the singlet and octet axial charges are identical (Eq. (20)). Taking a_8 from hyperon decay constants, they obtained $\Gamma_1^p = 0.185$ and $\Gamma_1^n = -0.023$ for the proton and the neutron, respectively. Unlike the Bjorken sum rule, the Ellis–Jaffe sum rules depend on several assumptions, in particular a vanishing polarisation of strange quarks in the nucleon.

4.2. Experimental method of the CERN experiments

The three CERN experiments by the EMC (1985), the SMC (1992–1996) and the COMPASS Collaboration (since 2002) share the same principle. All of them use the M2 beam line providing longitudinally polarised positive muons with momenta of up to 200 GeV. A polarisation of about 80% was measured by the SMC^{40,41} using two dedicated beam polarimeters. The solid-state polarised target consists of two or three cells with material of opposite polarisations, which are inverted at regular intervals. The open forward spectrometer and the polarised target are described in Sections 2.2 and 2.3.

The experiments measure the DIS cross-section asymmetry for parallel and anti-parallel orientation of muon and nucleon spins, taking advantage of the cancellation of several important quantities in the asymmetry: the dominant unpolarised cross-section, the beam flux, the number of target nuclei, and the spectrometer acceptance. From the measured DIS cross-section asymmetry the virtual-photon asymmetry

$$A_1 = \frac{\sigma_{\frac{1}{2}} - \sigma_{\frac{3}{2}}}{\sigma_{\frac{1}{2}} + \sigma_{\frac{3}{2}}} = \frac{g_1 - \frac{Q^2}{\nu^2} g_2}{F_1} \rightarrow \frac{g_1}{F_1} \quad (22)$$

is determined taking into account the beam and target polarisations, the fraction of polarisable nucleons in the target material and the depolarisation of the virtual photon with respect to the parent muon. Here $\sigma_{\frac{1}{2}}$ and $\sigma_{\frac{3}{2}}$ are the cross-sections for the absorption of a transversely polarised photon with spin antiparallel and parallel to the spin of the longitudinally polarised nucleon. The contribution of the structure

function g_2 is suppressed by Q^2/ν^2 and A_1 is essentially equal to the ratio of the spin-dependent and the spin-averaged structure functions g_1 and F_1 .

4.3. Experimental results

4.3.1. Sum rules

The EMC proton result $\Gamma_1^p = 0.126 \pm 0.010 \pm 0.015$ is in clear disagreement with the Ellis–Jaffe prediction of 0.185 ± 0.005 . From this the EMC deduced a small axial singlet charge of $a_0 = 0.098 \pm 0.076 \pm 0.113$ and a negative strange quark contribution to the proton spin of $\Delta s + \Delta \bar{s} = -0.095 \pm 0.016 \pm 0.023$.³⁴ Recent COMPASS results indicate a somewhat larger quark spin contribution of $a_0 = 0.33 \pm 0.03 \pm 0.05$ and a similar strange quark contribution $\Delta s + \Delta \bar{s} = -0.08 \pm 0.01 \pm 0.02$.⁴³ Still the original EMC conclusion that the quark spins do not account for most of the proton spin holds.

In 1992, the SMC performed the first measurement of the neutron g_1 structure function⁴⁴ using a polarised deuteron target and the EMC result for the proton. The measurement revealed a violation of the Ellis–Jaffe sum rule for the neutron and confirmed the Bjorken sum rule for the difference of proton and neutron first moments of g_1 (Eq. (21)). As for the deuteron, the measured x -range was subsequently extended also for the proton⁴⁵ down to $x = 0.004$ (for $Q^2 > 1 \text{ GeV}^2$) confirming essentially the EMC result.

Also in 1992, the ^3He experiment E142 at SLAC reported the contradicting findings: a validation of the Ellis–Jaffe sum rule for the neutron and thus a violation of the Bjorken sum rule.⁴⁶ Due to the lower beam energy of 19 GeV–26 GeV, E142 had to struggle with large QCD radiative corrections of order $\alpha_s(Q^2)/\pi$ for the Bjorken sum rule. From this Q^2 evolution Ellis and Karliner determined in 1994 the strong coupling constant $\alpha_s(M_Z^2) = 0.122_{-0.009}^{+0.005}$ using corrections up to order $(\alpha_s/\pi)^4$.⁴⁷ Applying these corrections, the E142 result turned out to be also compatible with the Bjorken sum rule.

The most recent COMPASS result for the Bjorken integral and for the isosinglet “Ellis–Jaffe” integral $\int_{x_{\min}}^1 (g_1^p + g_1^n) dx$ is shown in Fig. 6 as a function of the lower integration limit x_{\min} at $Q^2 = 3 \text{ GeV}^2$. Note that while for the Bjorken sum there is a large contribution for $x < 0.1$, the contribution from this region to the Ellis–Jaffe sum is negligible. With $a_3 = 1.28 \pm 0.07 \pm 0.010$ compared to the PDG value for $|g_A/g_V| = 1.2723 \pm 0.0023$ the Bjorken sum rule is confirmed at the 10% level.⁴²

4.3.2. Structure functions and quark helicity distributions

The spin-dependent structure function data for the proton as obtained from the asymmetry measurements using Eq. (22) are shown in Fig. 7 as a function of x and Q^2 . The world data come from COMPASS,^{42,43} SMC,⁴⁸ EMC,³⁴ SLAC,^{49–53} HERMES,⁵⁴ and Jefferson Lab.^{55,56} The smallest- x data were obtained by the CERN experiments. Similar data exist for the deuteron. HERMES, SLAC and Jefferson Lab also obtained some neutron (^3He) data.

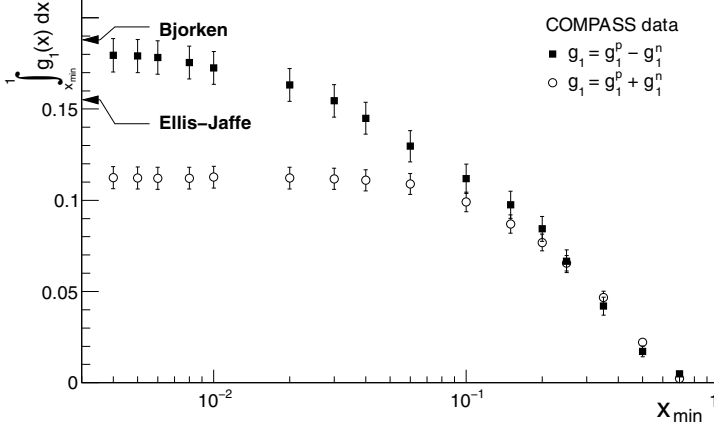


Fig. 6. Convergence of the first moments of $g_1^p \mp g_1^n$ as a function of the lower integration limit x_{\min} from the COMPASS proton and deuteron data.⁴² The arrows indicate the theoretical expectations. Error bars are statistical only.

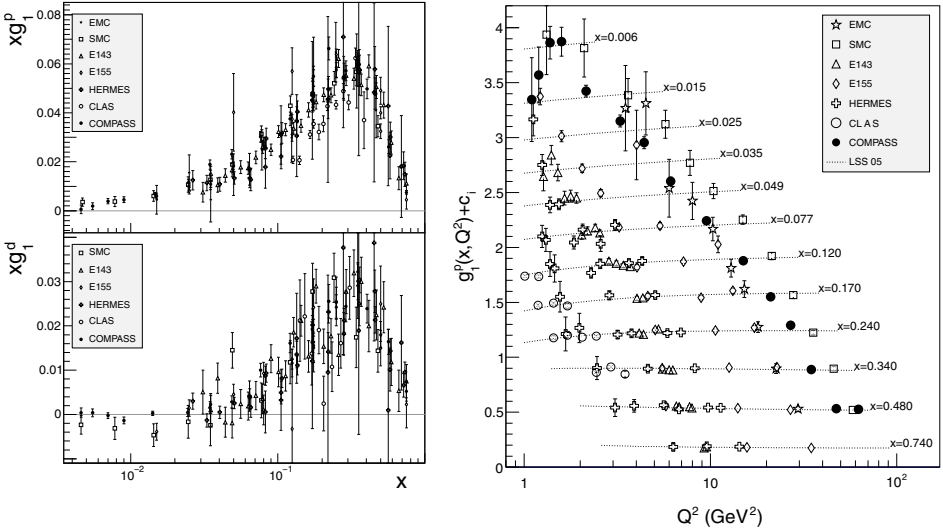


Fig. 7. Left: $xg_1(x, Q^2)$ as function of x with $Q^2 > 1 \text{ GeV}^2$ for the proton (top) and the deuteron (bottom). Right: Proton data for $g_1(x, Q^2)$ as a function of x and Q^2 with $W > 2.5 \text{ GeV}$. For clarity the g_1 data for the i -th x bin (starting from $i = 0$) were offset by $c_i = 0.28(11.6 - i)$. Error bars are statistical errors only.

Insight into the individual quark and gluon helicity distributions can be gained from semi-inclusive deep inelastic scattering (SIDIS, Fig. 8). The probability for a quark q of flavour i to fragment into a hadron h with energy fraction $z = E_h/\nu$ is described by the fragmentation function $D_i^h(z, Q^2)$. Due to the factorisation theorem, x and z dependences appear as a product of quark distribution and fragmentation functions. Similar to the inclusive asymmetries, one obtains double-spin

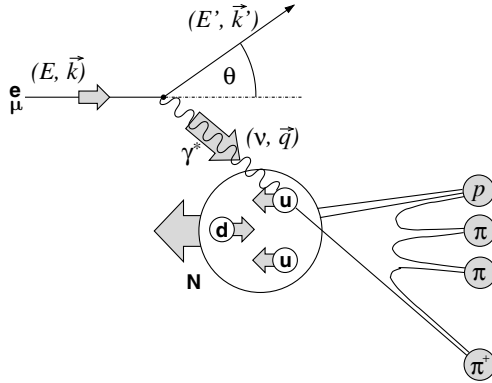


Fig. 8. Semi-inclusive deep inelastic scattering.

cross-section asymmetries for the production of a hadron h

$$A_1^h(x, Q^2, z) \simeq \frac{\sum_i e_i^2 \Delta q_i(x, Q^2) D_i^h(z, Q^2)}{\sum_i e_i^2 q_i(x, Q^2) D_i^h(z, Q^2)}. \quad (23)$$

An up quark preferentially fragments into a π^+ while a down quark favours fragmenting into a π^- . The difference of favoured and unfavoured fragmentation allows for a flavour separation of the quark helicity distributions. The first leading-order (LO) determination of the valence and nonstrange sea polarisation using this method was made by the SMC.⁵⁷ A recent result by COMPASS is shown in Fig. 9.

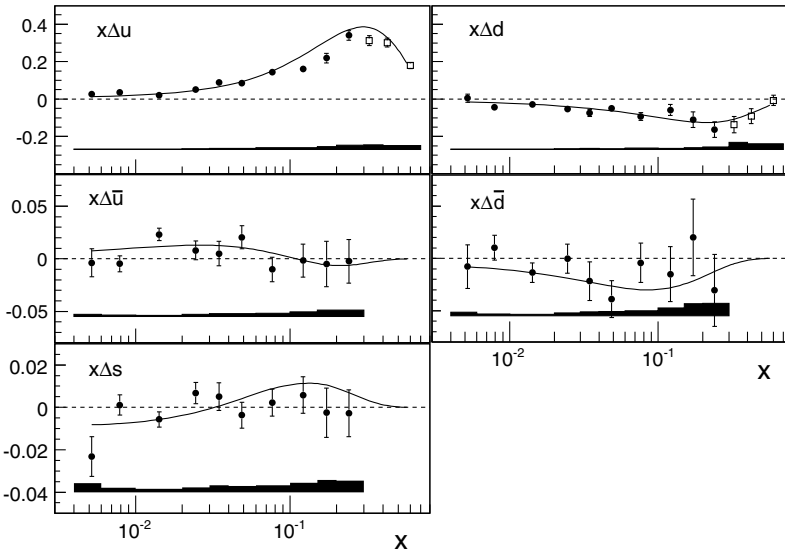


Fig. 9. Quark helicity distributions from a LO analysis.⁵⁸ The bands indicate the systematic uncertainty.

The up quark polarisation is positive and the one of the down quark negative. The strange quark polarisation is slightly positive contrary to the x -integrated result from the first moment of g_1 . This issue is still under discussion and may be linked to the uncertainties in the fragmentation functions for strange quarks.

4.3.3. Gluon helicity distributions

In 1988, it was shown that the gluon polarisation contributes via the axial anomaly to the singlet axial charge like

$$a_0 = \sum_q \Delta q - 3 \frac{\alpha_s}{2\pi} \Delta g \quad (24)$$

with $\alpha_s \Delta g$ constant, i.e. independent of Q^2 .^{61,62} This led to the suggestion that maybe a large positive gluon polarisation would mask the quark spin contribution to the nucleon spin. In order to recover the value of 0.6 for $\Delta\Sigma$, values of $2\hbar$ to $3\hbar$ are required for Δg . This gave birth to the COMPASS Collaboration, which set out to determine the gluon polarisation.

The gluon polarisation can be probed in SIDIS via the gluon-photon fusion process (PGF) $\gamma g \rightarrow q\bar{q}$. Particularly interesting is the production of open charm, e.g. of D mesons, because of the absence at small x of charmed quarks in the nucleon. Furthermore, high- p_T hadron pairs and single hadrons can be used to determine the gluon polarisation. The first indication that the gluon polarisation is much smaller then required by the anomaly scenario came 2005 from COMPASS⁶³ using events with high- p_T hadron pairs at low Q^2 . Later results from open charm⁶⁴ and events with high- p_T hadron pairs at $Q^2 > 1 \text{ GeV}^2$ followed.⁶⁵ The LO results of such determinations are summarised in Fig. 10. Results from RHIC confirmed the small gluon polarisation, but recently also indicated that the gluon still may contribute significantly to the nucleon spin.⁶⁶

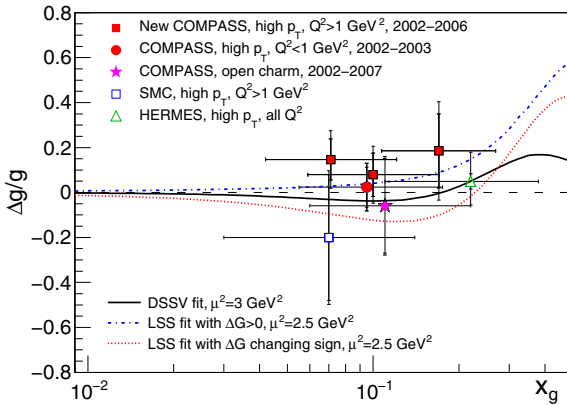


Fig. 10. Gluon polarisation $\Delta g/g$ from LO determinations as function of x_g . The horizontal error bar indicates the x range of the measurement. Also shown are the results from NLO QCD analyses of the world data.^{59,60}

4.3.4. Global QCD analyses

Like in the spin-averaged case (see Section 3.3), the Q^2 evolution of the g_1 structure function (Fig. 7) is described by the DGLAP equations.²⁵ From next-to-leading (NLO) QCD analyses one obtains the individual quark, antiquark and gluon helicity distributions $\Delta q(x, Q^2)$ and $\Delta g(x, Q^2)$. Modern global QCD analyses^{59,60,66} take into account inclusive DIS and SIDIS data as well as data from polarised pp collisions at RHIC. While the quark distributions are well determined, the gluon distribution still have considerable uncertainties owing to the small Q^2 range of the data for a given x . A polarised electron-ion collider would change this situation dramatically as HERA did in the unpolarised case.

4.4. Transverse spin

4.4.1. Transversity

Apart from the spin-averaged (F_1) and spin-dependent structure function (g_1), there is at leading twist a third, chiral-odd structure function h_1 describing the distribution of transverse quark spins in a transversely polarised nucleon

$$h_1(x) = \frac{1}{2} \sum_i e_i^2 \delta q_i(x) \quad \text{with} \quad \delta q_i(x) = q_i^\uparrow(x) - q_i^\downarrow(x), \quad (25)$$

where q^\uparrow and q^\downarrow respectively indicate the number densities of quarks with spin orientation parallel and antiparallel to the transverse nucleon spin. In the non-relativistic case $h_1(x)$ is equal to $g_1(x)$. This structure function does not contribute to inclusive scattering, because it implies a flip of the quark spin, which is conserved for massless quarks. However, in SIDIS h_1 can be coupled to the chirally odd Collins fragmentation function $\Delta_T D_i^h(z, p_T)$ and thus lead to an azimuthal sine modulation of the cross-section asymmetry in the Collins angle^b $\phi_{\text{Coll}} = \phi_h + \phi_S + \pi$ with an amplitude of

$$A_{\text{Coll}}(x, z) \sim \frac{\sum_i e_i^2 \delta q_i(x) \Delta_T D_i^h(z, p_T^h)}{\sum_q e_q^2 q_i(x) D_i^h(z, p_T^h)}. \quad (26)$$

Here p_T^h denotes the transverse hadron momentum with respect to the virtual photon; ϕ_h and ϕ_S are the azimuthal angles of the hadron and the nucleon spin. Figure 11 (top) shows the Collins asymmetry for the proton as measured for positive and negative hadrons (dominantly pions). Similar measurements exist for identified pions and kaons⁶⁷ and from HERMES. The corresponding asymmetries for the deuteron are compatible with zero due to a cancellation of the up and down quark contributions.

^bNote that some experiments, e.g. HERMES, use a definition of ϕ_{Coll} without adding π .

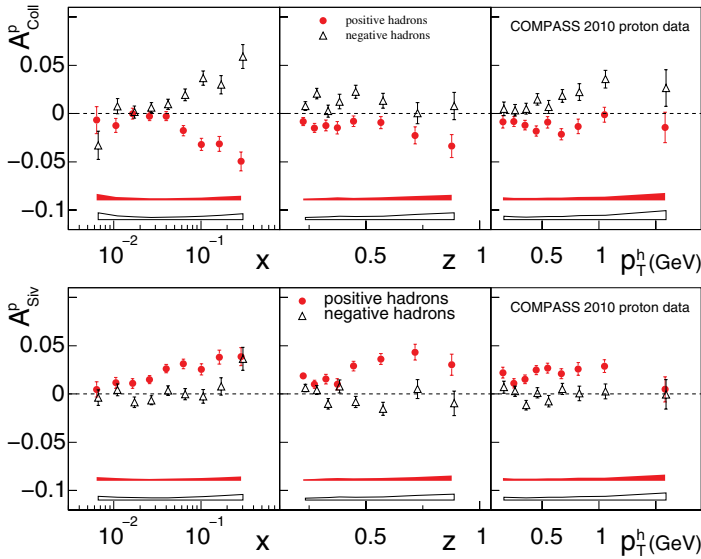


Fig. 11. Collins (top) and Sivers (bottom) asymmetry^{68,69} of the proton for positive and negative hadrons as functions of x , z , and p_T^h from COMPASS. The bands indicate the systematic uncertainty.

Transversity can — instead of to the Collins function — also couple to another chiral-odd fragmentation function, the interference fragmentation function (IFF), which generates a pair of oppositely charged hadrons. The similarity of the Collins asymmetry (for positive hadrons) and the 2-hadron asymmetry suggests that a common mechanism is at work in both cases (Fig. 12).

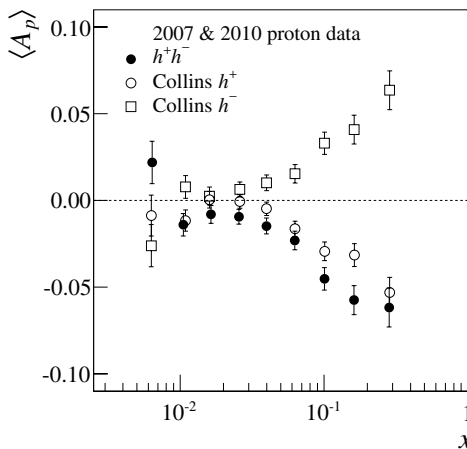


Fig. 12. Collins asymmetries for positive (lower open circles) and negative hadrons (upper open circles) and 2-hadron asymmetries (full circles) as function of x .^{68,70}

Phenomenological determinations of the transversity structure function⁷¹ have been made using data from COMPASS, HERMES, and Belle. At Belle, the Collins and IFF fragmentation function have been measured in e^+e^- collisions. These analyses show a positive transverse polarisation of the up quarks and a negative one for down quarks in a transversely polarised nucleon.

4.4.2. Transverse-momentum-dependent parton distributions

The PDFs discussed so far do not explain the strong transverse single-spin asymmetries observed in both hadron and DIS reactions indicating significant spin-orbit coupling in the nucleon associated with the quark transverse momentum k_T . Transverse-momentum-dependent (TMD) distributions allow for such a k_T dependence in addition to the one on the longitudinal momentum fraction x carried by the parton. In QCD there are eight leading-twist transverse-momentum-dependent parton distributions listed below.

N \ q	U	L	T
U	f_1		h_1^\perp
L		g_1	h_{1L}^\perp
T	f_{1T}^\perp	g_{1T}^\perp	h_1 h_{1T}^\perp

Here U, L, and T stand for unpolarised, longitudinally polarised, and transversely polarised nucleons (rows) and quarks (columns), respectively. Upon integration over k_T the TMD PDFs in the diagonal (in bold) yield the usual structure functions $F_1(x)$, $g_1(x)$, and $h_1(x)$, while all off-diagonal TMD PDFs vanish.

The best known TMD PDF is the Sivers function f_{1T}^\perp which describes the distribution of unpolarised quarks in a transversely polarised nucleon. It couples to the standard unpolarised fragmentation function D_i^h and causes an azimuthal asymmetry in $\sin \phi_{\text{Siv}}$, where the Sivers angle is defined by $\phi_{\text{Siv}} = \phi_h - \phi_S$. Figure 11 (bottom) shows the Sivers asymmetry of the proton for positive and negative hadrons. For positive hadrons a clear positive asymmetry is visible, in particular at larger x and z . The Boer–Mulders function h_1^\perp describes the distribution of transversely polarised quarks in an unpolarised nucleon and couples to the Collins fragmentation function. As the Sivers function, the Boer–Mulders function is odd under time reversal and only nonvanishing due to initial or final-state interactions. For these functions only a restricted universality is predicted implying a change of sign when going from SIDIS to Drell–Yan (DY) reactions

$$f_{1T}^\perp|_{\text{SIDIS}} = -f_{1T}^\perp|_{\text{DY}} \quad \text{and} \quad h_1^\perp|_{\text{SIDIS}} = -h_1^\perp|_{\text{DY}}. \quad (27)$$

An experimental test of this prediction is an important next step in spin physics.

COMPASS has the unique possibility to measure with the same spectrometer the sign change of the T -odd Sivers and Boer–Mulders PDFs in the upcoming, first-ever polarised Drell–Yan experiment with a pion beam planned for 2015.

4.4.3. Generalised parton distributions

The role of the orbital angular momentum in the nucleon is still unclear and the only known access to this quantity is via generalised parton distribution functions (GPD),⁷² which correlate longitudinal momentum and transverse spatial degrees of freedom. They enter in the cross-sections for deeply virtual Compton scattering and hard exclusive meson production. COMPASS started to study these processes and in 2016/17 will have GPD runs with a 2.5 m long liquid hydrogen target.

5. Conclusions

Deep inelastic muon scattering at the SPS has been a unique success story for more than 35 years now, and has grown into the most long-lived experimental programme of CERN. It has had a fundamental impact on the present-day understanding of the innermost structure of hadronic matter, and has been an important and fruitful testing ground for the Quark–Parton Model and for Quantum Chromodynamics, which it helped establishing as the universally accepted theory of the strong interaction of quarks and gluons. It has even outlived the HERA electron–proton collider programme at DESY, which had some of its major roots in the CERN muon experiments.

The question whether deep inelastic lepton scattering has a future after COMPASS and HERA cannot be answered today. Only the discovery of a substructure of quarks or leptons would warrant the investment in a major new programme; by colliding protons from the LHC — or a future hadron collider of even higher energy — with a new, high-energy electron beam, CERN would be well equipped to repeat the successes of its deep inelastic scattering programmes at a new energy frontier.

References

1. W. Panofsky, Electromagnetic interactions: Low q^2 electrodynamics: Elastic and inelastic electron (and muon) scattering, in *Proc. 14th Int. Conf. on High-Energy Physics*, Vienna, 1968.
2. M. Gell-Mann, *Phys. Lett.* **8**, 214–215 (1964), doi: 10.1016/S0031-9163(64)92001-3.
3. G. Zweig, An SU(3) model for strong interaction symmetry and its breaking (Version 2), CERN-TH-412 (1964).
4. J. Aubert *et al.*, *Phys. Lett. B* **123**, 275 (1983), doi: 10.1016/0370-2693(83)90437-9.
5. R. Clift and N. Doble, Proposed design of a high-energy, high intensity muon beam for the SPS north experimental area (1974), CERN/LAB. II/EA/74-2, CERN/SPSC/74-12.
6. J. Aubert *et al.*, *Nucl. Instrum. Meth.* **179**, 445–466 (1981), doi: 10.1016/0029-554X(81)90169-5.

7. J. Aubert *et al.*, *Nucl. Phys. B* **259**, 189 (1985), doi: 10.1016/0550-3213(85)90635-2.
8. J. Albanese *et al.*, *Nucl. Instrum. Meth.* **212**, 111 (1983), doi: 10.1016/0167-5087(83)90682-8.
9. D. Bollini *et al.*, *Nucl. Instrum. Meth.* **204**, 333 (1983), doi: 10.1016/0167-5087(83)90063-7.
10. A. Benvenuti *et al.*, *Nucl. Instrum. Meth. A* **226**, 330 (1984), doi: 10.1016/0168-9002(84)90045-7.
11. P. Amaudruz *et al.*, *Z. Phys. C* **51**, 387–394 (1991), doi: 10.1007/BF01548560.
12. P. Abbon *et al.*, *Nucl. Instrum. Meth. A* **577**, 455–518 (2007), doi: 10.1016/j.nima.2007.03.026.
13. P. Abbon *et al.*, The COMPASS setup for physics with hadron beams, arXiv:hep-ex/1410.1797.
14. A. Argento *et al.*, *Phys. Lett. B* **120**, 245 (1983), doi: 10.1016/0370-2693(83)90665-2.
15. A. Argento *et al.*, *Phys. Lett. B* **140**, 142 (1984), doi: 10.1016/0370-2693(84)91065-7.
16. F. Halzen and A. D. Martin, *Quarks and Leptons* (Wiley, 1984), ISBN 9780471887416.
17. R. Roberts, *The Structure of the Proton: Deep Inelastic Scattering* (Cambridge Monographs on Mathematical Physics) (Cambridge University Press, 1990).
18. E. D. Bloom *et al.*, *Phys. Rev. Lett.* **23**, 930–934 (1969), doi: 10.1103/PhysRevLett.23.930.
19. M. Breidenbach *et al.*, *Phys. Rev. Lett.* **23**, 935–939 (1969), doi: 10.1103/PhysRevLett.23.935.
20. J. Bjorken, *Phys. Rev.* **179**, 1547–1553 (1969), doi: 10.1103/PhysRev.179.1547.
21. A. Benvenuti *et al.*, *Phys. Lett. B* **223**, 485 (1989), doi: 10.1016/0370-2693(89)91637-7.
22. M. Arneodo *et al.*, *Phys. Lett. B* **364**, 107–115 (1995), doi: 10.1016/0370-2693(95)01318-9.
23. L. Whitlow, E. Riordan, S. Dasu, S. Rock and A. Bodek, *Phys. Lett. B* **282**, 475–482 (1992), doi: 10.1016/0370-2693(92)90672-Q.
24. M. Adams *et al.*, *Phys. Rev. D* **54**, 3006–3056 (1996), doi: 10.1103/PhysRevD.54.3006.
25. G. Altarelli and G. Parisi, *Nucl. Phys. B* **126**, 298 (1977), doi: 10.1016/0550-3213(77)90384-4.
26. A. Benvenuti *et al.*, *Phys. Lett. B* **195**, 97 (1987), doi: 10.1016/0370-2693(87)90892-6.
27. A. Benvenuti *et al.*, *Phys. Lett. B* **223**, 490 (1989), doi: 10.1016/0370-2693(89)91638-9.
28. A. Benvenuti *et al.*, *Phys. Lett. B* **237**, 592 (1990), doi: 10.1016/0370-2693(90)91231-Y.
29. M. Virchaux and A. Milsztajn, *Phys. Lett. B* **274**, 221–229 (1992), doi: 10.1016/0370-2693(92)90527-B.
30. R. K. Ellis, W. Furmanski and R. Petronzio, *Nucl. Phys. B* **212**, 29 (1983), doi: 10.1016/0550-3213(83)90597-7.
31. S. I. Alekhin, Combined analysis of SLAC-BCDMS-NMC data at high x : α_s and high twists, arXiv:hep-ph/9907350.
32. Particle Data Group (K. Olive *et al.*), *Chin. Phys. C* **38**, 090001 (2014), doi: 10.1088/1674-1137/38/9/090001.
33. J. Ashman *et al.*, *Phys. Lett. B* **206**, 364 (1988), doi: 10.1016/0370-2693(88)91523-7.
34. J. Ashman *et al.*, *Nucl. Phys. B* **328**, 1 (1989), doi: 10.1016/0550-3213(89)90089-8.
35. E. Leader and M. Anselmino, *Z. Phys. C* **41**, 239 (1988), doi: 10.1007/BF01566922.
36. C. A. Aidala *et al.*, *Rev. Mod. Phys.* **85**, 655–691 (2013), doi: 10.1103/RevModPhys.85.655.
37. J. Bjorken, *Phys. Rev.* **148**, 1467–1478 (1966), doi: 10.1103/PhysRev.148.1467.
38. J. Bjorken, *Phys. Rev. D* **1**, 1376–1379 (1970), doi: 10.1103/PhysRevD.1.1376.

39. J. R. Ellis and R. L. Jaffe, *Phys. Rev. D* **9**, 1444 (1974), doi: 10.1103/PhysRevD.10.1669.2, 10.1103/PhysRevD.9.1444.
40. B. Adeva *et al.*, *Nucl. Instrum. Meth. A* **343**, 363–373 (1994), doi: 10.1016/0168-9002(94)90213-5.
41. D. Adams *et al.*, *Nucl. Instrum. Meth. A* **443**, 1–19 (2000), doi: 10.1016/S0168-9002(99)01017-7.
42. M. Alekseev *et al.*, *Phys. Lett. B* **690**, 466–472 (2010), doi: 10.1016/j.physletb.2010.05.069.
43. V. Y. Alexakhin *et al.*, *Phys. Lett. B* **647**, 8–17 (2007), doi: 10.1016/j.physletb.2006.12.076.
44. B. Adeva *et al.*, *Phys. Lett. B* **302**, 533–539 (1993), doi: 10.1016/0370-2693(93)90438-N.
45. D. Adams *et al.*, *Phys. Lett. B* **329**, 399–406 (1994), doi: 10.1016/0370-2693(94)90793-5.
46. P. Anthony *et al.*, *Phys. Rev. Lett.* **71**, 959–962 (1993), doi: 10.1103/PhysRevLett.71.959.
47. J. R. Ellis and M. Karliner, *Phys. Lett. B* **341**, 397–406 (1995), doi: 10.1016/0370-2693(95)80021-O.
48. B. Adeva *et al.*, *Phys. Rev. D* **58**, 112001 (1998), doi: 10.1103/PhysRevD.58.112001.
49. P. Anthony *et al.*, *Phys. Rev. D* **54**, 6620–6650 (1996), doi: 10.1103/PhysRevD.54.6620.
50. K. Abe *et al.*, *Phys. Rev. Lett.* **79**, 26–30 (1997), doi: 10.1103/PhysRevLett.79.26.
51. K. Abe *et al.*, *Phys. Rev. D* **58**, 112003 (1998), doi: 10.1103/PhysRevD.58.112003.
52. P. Anthony *et al.*, *Phys. Lett. B* **463**, 339–345 (1999), doi: 10.1016/S0370-2693(99)00940-5.
53. P. Anthony *et al.*, *Phys. Lett. B* **493**, 19–28 (2000), doi: 10.1016/S0370-2693(00)01014-5.
54. A. Airapetian *et al.*, *Phys. Rev. D* **75**, 012007 (2007), doi: 10.1103/PhysRevD.75.012007.
55. X. Zheng *et al.*, *Phys. Rev. Lett.* **92**, 012004 (2004), doi: 10.1103/PhysRevLett.92.012004.
56. K. Dharmawardane *et al.*, *Phys. Lett. B* **641**, 11–17 (2006), doi: 10.1016/j.physletb.2006.08.011.
57. B. Adeva *et al.*, *Phys. Lett. B* **369**, 93–100 (1996), doi: 10.1016/0370-2693(95)01584-1.
58. M. Alekseev *et al.*, *Phys. Lett. B* **693**, 227–235 (2010), doi: 10.1016/j.physletb.2010.08.034.
59. D. de Florian *et al.*, *Phys. Rev. D* **80**, 034030 (2009), doi: 10.1103/PhysRevD.80.034030.
60. E. Leader, A. V. Sidorov and D. B. Stamenov, *Phys. Rev. D* **82**, 114018 (2010), doi: 10.1103/PhysRevD.82.114018.
61. G. Altarelli and G. G. Ross, *Phys. Lett. B* **212**, 391 (1988), doi: 10.1016/0370-2693(88)91335-4.
62. A. Efremov and O. Teryaev, Spin structure of the nucleon and triangle anomaly, *Nucl. Phys.* (1988).
63. E. Ageev *et al.*, *Phys. Lett. B* **633**, 25–32 (2006), doi: 10.1016/j.physletb.2005.11.049.
64. C. Adolph *et al.*, *Phys. Rev. D* **87**(5), 052018 (2013), 10.1103/PhysRevD.87.052018.
65. C. Adolph *et al.*, *Phys. Lett. B* **718**, 922–930 (2013), doi: 10.1016/j.physletb.2012.11.056.
66. D. de Florian *et al.*, *Phys. Rev. Lett.* **113**, 012001 (2014), doi: 10.1103/PhysRevLett.113.012001.

67. C. Adolph *et al.*, Collins and Sivers asymmetries in muon production of pions and kaons off transversely polarised proton, arXiv:hep-ex/1408.4405.
68. C. Adolph *et al.*, *Phys. Lett. B* **717**, 383–389 (2012), doi: 10.1016/j.physletb.2012.09.056.
69. C. Adolph *et al.*, *Phys. Lett. B* **717**, 376–382 (2012), doi: 10.1016/j.physletb.2012.09.055.
70. C. Adolph *et al.*, *Phys. Lett. B* **736**, 124–131 (2014), doi: 10.1016/j.physletb.2014.06.080.
71. M. Anselmino *et al.*, *Phys. Rev. D* **87**, 094019 (2013), doi: 10.1103/PhysRevD.87.094019.
72. X.-D. Ji, *Phys. Rev. Lett.* **78**, 610–613 (1997), doi: 10.1103/PhysRevLett.78.610.